

## Literature Search and Review

Doug Auld, Anton Simeonov, Wendy Lea, and Craig Thomas

National Institutes of Health Bethesda, Maryland.

---

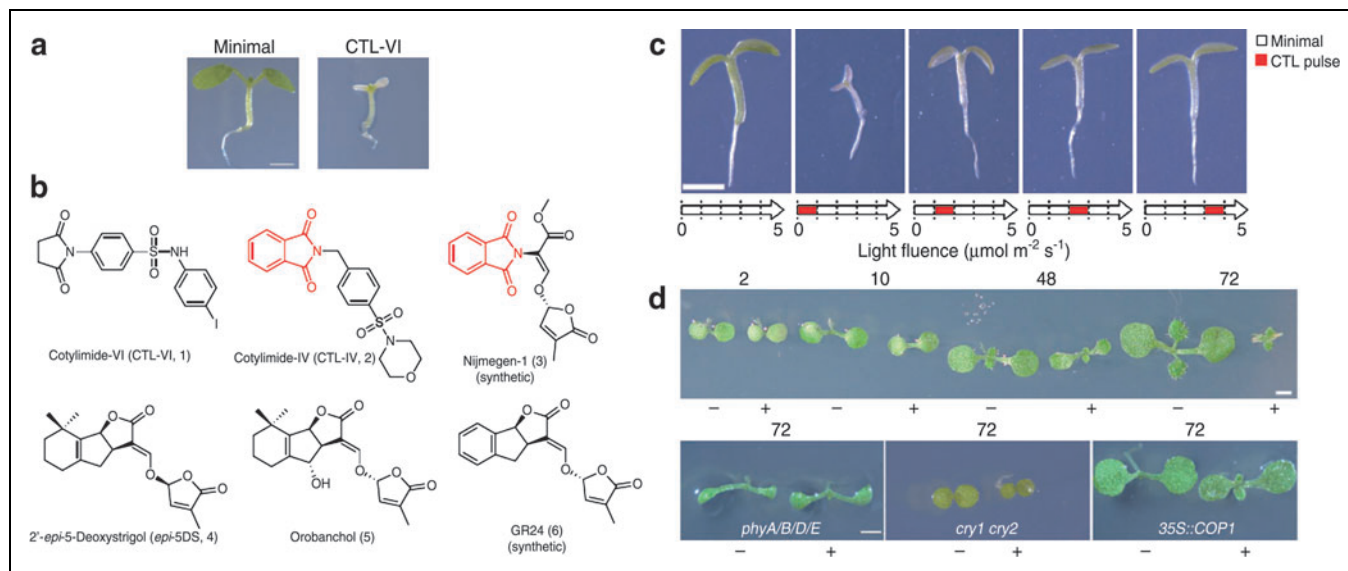
### WEED TARGETS

Tsuchiya Y, Vidaurre D, Toh S, Hanada A, Nambara E, Kamiya Y, Yamaguchi S, McCourt P. A small-molecule screen identifies new functions for the plant hormone strigolactone. *Nat Chem Biol* 6;2010:741–749.

**Abstract:** Parasitic weeds of the genera *Striga* and *Orobanche* are considered the most damaging agricultural agents in the developing world. An essential step in parasitic seed germination is sensing a group of structurally related compounds called strigolactones that are released by host plants. Although this makes strigolactone synthesis and action a major target of biotechnology, little fundamental information is known about this hormone. Chemical genetic screening using *Arabidopsis thaliana* as a platform identified a collection of related small molecules, cotylimides, which perturb strigolactone accumulation. Suppressor screens against select cotylimides identified light-signaling genes as positive regulators of strigolactone levels. Molecular analysis showed strigolactones regulate the nuclear localization of the COP1 ubiquitin ligase, which in part determines the levels of light regulators such as HY5. This information not only uncovers new functions for strigolactones but was also used to identify rice cultivars with reduced capacity to germinate parasitic seed.

**Commentary:** The use of small molecules to understand an uncharacterized biological pathway is nicely illustrated in this article. Strigolactones are a class of plant hormones that normally regulate the branching patterns of plants. In the root, these hormones

stimulate beneficial interactions between the root and certain fungi, and nearly 80% of plants require this interaction for growth. However, certain parasitic plant species, such as *Striga*, known as “witchweed,” have pirated these hormones to awaken their dormant seeds, leading to devastation of the host plant. In Africa, witchweed affects >300 million people through disruption of the food supply. The development of synthetic strigolactones that could fool the parasitic seeds into germinating in the absence of the host plant would be an enormous benefit to agriculture in affected regions, including Australia and countries in Africa and Asia. Here, an assay for seed dormancy and leaf development was developed in the *Arabidopsis* plant and used to screen 10,000 compounds from the Cambridge DIVERSet collection. This identified a group of structurally related compounds that all inhibited cotyledon growth (termed cotylimides or CTLs; see **figure**). These compounds showed effects on the light-dependent process of seedlings in which the cotyledons are emerging and beginning to green. Studies in mutant *Arabidopsis* linked this phenotype to a ubiquitin ligase known as COP1 (Constitutive Photomorphogenic 1) known to inhibit the light response. The CTLs were also found to increase strigolactone levels, and the bleaching effect observed in emerging cotyledons is consistent with the phenotype upon treatment of a synthetic strigolactone (GR24, see **figure**). The authors then screened mutagenized seeds for the bleaching phenotype and identified 246 suppressor lines. It was noted that these lines showed a poor germination phenotype that could be rescued by CTL VI (shown in **figure**) or GR24, an activity that is akin to the role strigolactones play in parasitic plant seed



Structures and action of CTL compounds. **(a)** Five-day-old wild-type seedlings grown in the presence or absence of  $2.5 \mu\text{M}$  CTL-VI. **(b)** Chemical structures of CTL compounds and various natural and synthetic strigolactones. The dicyclic ring containing two ketone moieties shared between Nijmegen-1 and CTL-IV is shown in red. **(c)** Time frame of CTL-VI action on germinating wild-type seedlings. The arrows represent a 5-day period, with each day represented by a dashed line. The red box represents the time of exposure to CTL-VI. The pictures are of 5-day-old seedlings. **(d)** CTL-VI bleaching versus light fluence. Top, 5-day-old seedlings grown in the absence (–) or presence (+) of  $2.5 \mu\text{M}$  CTL-VI under different light intensities. Bottom, 5-day-old mutant seedlings defective in phytochrome perception (*phyA phyB phyD phyE*, abbreviated *phyA/B/D/E*), defective in cryptochrome perception (*cry1 cry2*) or over-expression COP1 ( $35S < COP1$ ), grown in the absence (–) or presence (+) of  $2.5 \mu\text{M}$  CTL-VI at a light fluence ( $72 \mu\text{mol m}^{-2} \text{s}^{-1}$ ) that bleaches wild-type cotyledons. Scale bars in a,c,d, 1 mm.

germination. Several genes involved in strigolactones signaling were identified in this work and a model pathway is described. Further study of the CTL compounds identified in this study in combination with genetic models should reveal additional mechanisms of stri-

golactone biosynthesis and regulation. Additionally, the specific genes already uncovered in this study could be used to create plant varieties that produce reduced levels of strigolactones. Contributed by Doug Auld.

## KINASE PROFILING KNOTS

Jester BW, Cox KJ, Gaj A, Shomin CD, Porter JR, Ghosh I. A coiled-coil enabled split-luciferase three-hybrid system: applied toward profiling inhibitors of protein kinases. *J Am Chem Soc* 2010;132:11727–11735.

**Abstract:** The 518 protein kinases encoded in the human genome are exquisitely regulated and their aberrant function(s) are often associated with human disease. Thus, in order to advance thera-

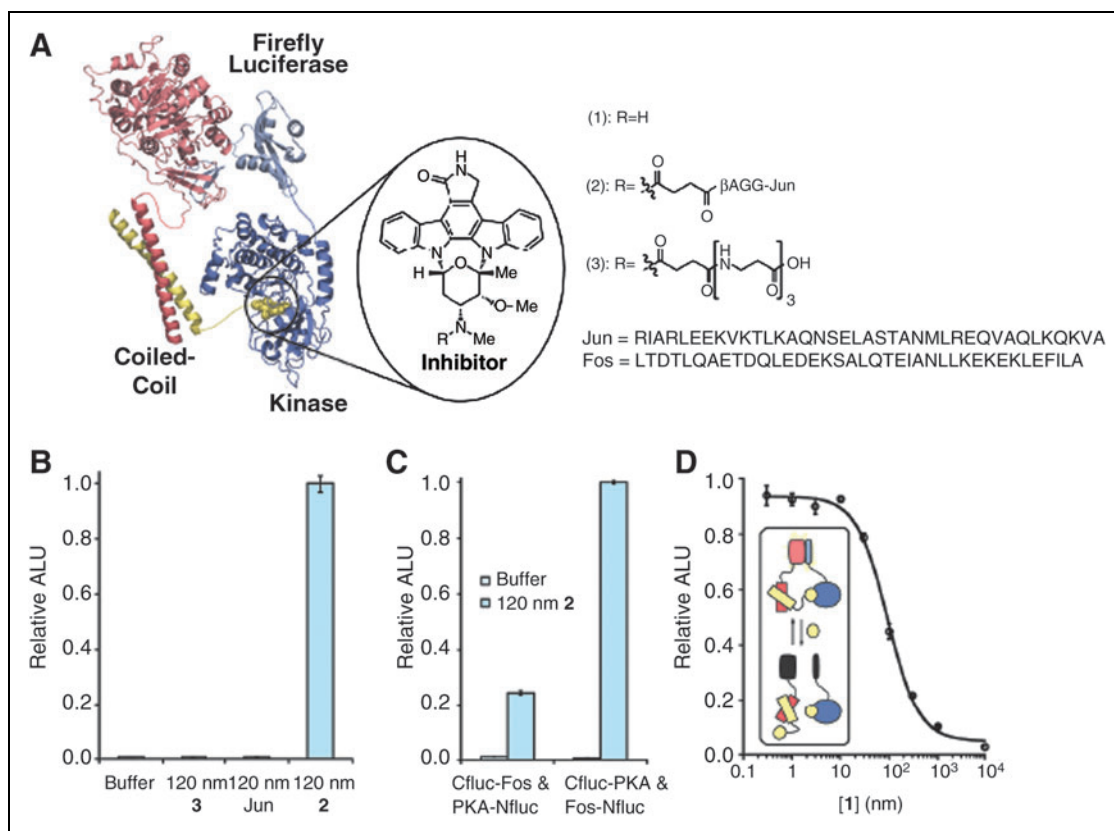
peutics and to probe signal transduction cascades, there is considerable interest in the development of inhibitors that can selectively target protein kinases. However, identifying specific compounds against such a large array of protein kinases is difficult to routinely achieve utilizing traditional activity assays, where purified protein kinases are necessary. Toward a simple, rapid, and practical method for identifying specific inhibitors, we describe the development and application of a split-protein methodology utilizing a

## LITERATURE SEARCH AND REVIEW

coiled-coil-assisted three hybrid system. In this approach, a protein kinase of interest is attached to the C-terminal fragment of split firefly luciferase and the coiled-coil Fos, which is specific for the coiled-coil Jun, is attached to the N-terminal fragment. Upon addition of Jun conjugated to a pan-kinase inhibitor such as staurosporine, a three-hybrid complex is established with concomitant reassembly of the split-luciferase enzyme. An inhibitor can be potentially identified by the commensurate loss in split-luciferase activity by displacement of the modified staurosporine. We demonstrate that this new three-hybrid approach is potentially general by testing protein kinases from the different kinase families. To interrogate whether this method allows for screening inhibitors, we tested six different protein kinases against a library of 80 known protein kinase inhibitors. Finally, we demonstrate that this three-hybrid system can potentially provide a rapid method for structure/function analysis as well as aid in the identification of allosteric inhibitors.

**Commentary:** Firefly luciferase (FLuc) has been used as both a reporter and as a sensor of intracellular messengers by constructing circularly permuted luciferases (see Fan and Wood, *ADDT* 2007;5:127–136). This article exploits a common motif in oncoproteins, such as c-Fos and c-Jun, that contains prototypical coiled-coil domains to obtain a bioluminescence assay for protein kinase inhibitors. Coiled-coil domains are an important structural motif in proteins in which two helices wind together forming dimers or trimers. The work described in this article uses a split

FLuc enzyme, expressed in reticulocyte lysate, where the N-terminal fragment of FLuc is attached to a coiled-coil domain of c-Fos and the C-terminal FLuc fragment is attached to the protein kinase of interest. To construct an active FLuc enzyme, the cognate coiled-coil domain of c-Jun is conjugated to staurosporine and added to the translation reaction, which results in a three-protein knot and reconstruction of active FLuc (see figure). In the assay, the c-Jun-staurosporine fusion acts as a chemical inducer of dimerization (CID) by binding to the ATP pocket of the kinase of interest while the c-Jun domain binds to the c-Fos domain. Compounds competitive with staurosporine disrupt this interaction, leading to a loss of FLuc activity. Using the catalytic domain of PKA for testing the system, it was found that the activity of FLuc depended on the



Proof-of-principle studies for the split-luciferase three-hybrid system. **(A)** A to-scale model of reassembled ternary complex with kinase domain from PKA. Split fragments of luciferase appended to the coiled-coil Fos and the kinase domain are brought into proximity through interactions of the CID (2), where the coiled-coil, Jun, binds Fos and staurosporine (1) binds the active site of PKA. **(B)** Luminescence after addition of either  $\text{St}_3\text{A}$  (3), Jun, or 2 to a translation containing Cfluc-PKA and Fos-Nfluc. **(C)** Domain swapped fusions of PKA and Fos to Cfluc and Nfluc were tested for luminescence upon addition of 2. **(D)** Concentration-dependent loss of luminescence upon addition of 1 to the preformed ternary complex demonstrating reversibility of the split-luciferase system.

addition of the CID resulting in a >100-fold enhancement in FLuc activity.  $IC_{50}$  measurements of staurosporine showed sigmoidal curves with potency values approximately fivefold higher than reported  $K_D$  values—likely due to the concentration of the CID coupled with the affinity of two halves of FLuc. The authors then expanded the study to test 10 additional protein kinases representing the seven different branches of the kinome. All of these showed a suitable increase in FLuc activity upon the addition of the CID. The assay system was further validated by paneling the Tocriscreen Kinase Inhibitor Toolbox (at 10  $\mu$ M) to measure the inhibitor selectivity profile. Of the 80 inhibitors tested, nine were also run in the Ambit assay (see ADDT commentary “Expanding the Kinome Inhibitor Selectivity Atlas.” 2008;6:9) and 17 had been assayed in radiometric enzymatic profile assays. The results obtained with the three-hybrid split FLuc system mirrored the published results with some discrepancies that may be due to choice of ATP concentration in the assay. The reticulocyte extracts

used for the assay can have endogenous protein kinases that could phosphorylate and activate certain kinases. Activating mutations (e.g., Ser to Asp or Glu) in the activation domains of PAK1 and AKT2 showed a more robust luminescence response to CID addition than the wild-type counterparts suggesting that these kinases are not fully activated in the lysate. Using known allosteric inhibitors of AKT1/2 the authors were able to show different inhibition values for assays based on the full-length kinase versus those containing only the catalytic domain, suggesting that this assay can be used to determine the mechanism of action of kinase inhibitors. The assay can be performed in as little ~3 hours using stored mRNA. Further, to flag direct FLuc inhibitors, the authors suggest that an orthogonal assay system could be constructed based on a split  $\beta$ -lactamase reporter. Bioluminescence is a very sensitive and facile assay detection format and the assay system described here could become a widely applicable platform to study enzyme/small molecule binding. Contributed by Doug Auld.

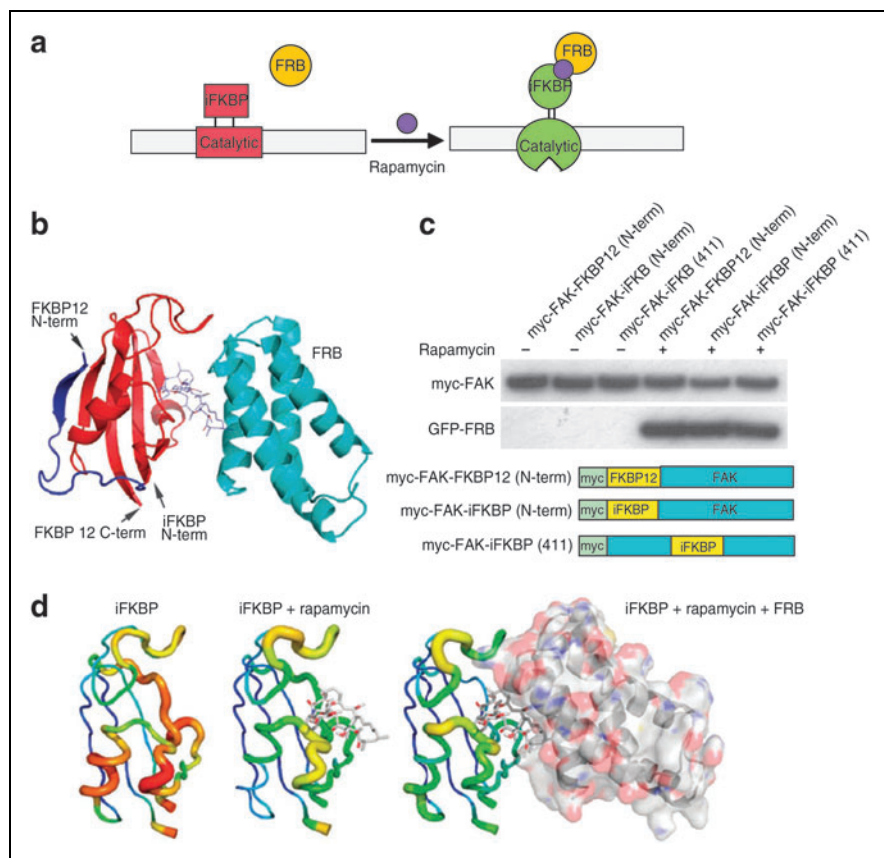
## KINASE ACTIVATION RAP

Karginov AV, Ding F, Kota P, Dokholyan NV, Hahn KM. Engineered allosteric activation of kinases in living cells. *Nat Biotechnol* 2010;28:743–748.

**Abstract:** Studies of cellular and tissue dynamics benefit greatly from tools that can control protein activity with specificity and precise timing in living systems. Here we describe an approach to confer allosteric regulation specifically on the catalytic activity of protein kinases. A highly conserved portion of the kinase catalytic domain is modified with a small protein insert that inactivates catalytic activity but does not affect other protein functions. Catalytic activity is restored by addition of rapamycin or non-immunosuppressive rapamycin analogs. Molecular modeling and mutagenesis indicate that the protein insert reduces activity by increasing the flexibility of the catalytic domain. Drug binding restores activity by increasing rigidity. We demonstrate the approach by specifically activating focal adhesion kinase (FAK) within minutes in living cells and show that FAK is involved in the regulation of membrane dynamics. Successful regulation of Src and p38 by insertion of the rapamycin-responsive element at the same

conserved site used in FAK suggests that our strategy will be applicable to other kinases.

**Commentary:** Chemical genetic approaches have been used to study the function of protein kinases in cellular systems (see for example ADDT 2006;4(3):241 and “Kinase Profiling Knots” commentary in this issue). This article uses the focal adhesion kinase (FAK) as a model to engineer a kinase that is selectively activated by rapamycin. A version of the small rapamycin-binding protein FKBP12 (iFKBP) was made that could be genetically inserted into a kinase sequence without affecting the rapamycin binding affinity. When iFKBP was inserted near the catalytic site of the kinase the activity of the enzyme was reduced but restored when rapamycin was added due to conformational changes within the iFKBP domain (the new sensor kinase was called RapR-FAK; see figure). Optimization efforts resulted in an FAK for which the activity could be regulated by the FKBP12-rapamycin binding protein (FRB). Co-expression of RapR-FAK with FRB in cells followed by treatment with 50 nM rapamycin for 2 minutes resulted in activation of the kinase as determined by the presence of phosphorylated parillin, a substrate of FAK. Analysis of several functions of FAK in cells showed that known FAK functions were



**Design and generation of RapR-FAK.** (a) Schematic representation of the approach used to regulate the catalytic activity of FAK. A fragment of FKBP is inserted at a position in the catalytic domain where it abrogates catalytic activity. Binding to rapamycin and FRB restores activity. (b) The truncated fragment of human FKBP12 (amino acids Thr22 through Glu108) inserted into the kinase domain. Blue and red, full-length FKBP12; red, proposed structure of the inserted fragment. The FKBP12 is shown in complex with rapamycin and FRB (cyan). (c) Immunoblot analysis of iFKBP interaction with rapamycin and FRB. Myc-tagged FKBP12 and iFKBP constructs were immunoprecipitated from cells treated for 1 hour with either 200 nM rapamycin or ethanol (solvent control). Co-immunoprecipitation of co-expressed GFP-FRB was detected using anti-GFP antibody. (d) Changes in the molecular dynamics of iFKBP upon binding to rapamycin and FRB. Warmer colors and thicker backbone indicate increasing root mean square fluctuation.

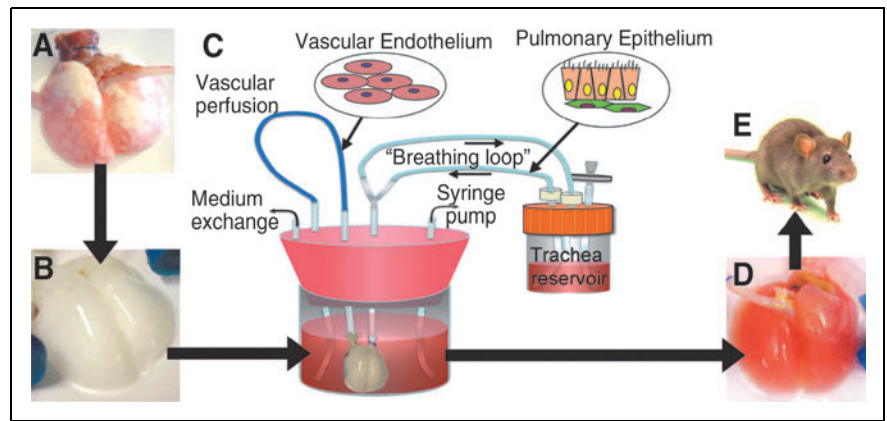
maintained in RapR-FAK. Next, the authors searched for additional phenotypes that depended on the activation of FAK, using the newly design sensor kinase. This study points to FAK stimulating Src protein kinase leading to dorsal ruffles in the cytoplasmic membrane, a structure that is thought to be important for cancer cell migration, and supports the finding that increased expression of FAK can lead to higher invasiveness of tumor cells. The method described here appears applicable to other kinases and both Src and P38 rapamycin sensitive kinases are described in the present work. The authors speculate from molecular dynamic simulations that insertion of the iFKBP near a structure that is critical for binding the ATP phosphate groups within the active site of the kinase is the reason for modulation of kinase catalytic activity. The efficiency of phosphate transfer reaction is reduced due to the greater conformational flexibility from the iFKBP domain. Binding of rapamycin to the iFKBP domain increases the conformational rigidity, thus stabilizing the phospho-transfer reaction and rescuing the kinase activity. The use of non-immunosuppressive rapamycin analogs could make the method suitable for in vivo studies. This study demonstrates how the same compound can be used as both a drug and a basic research tool to understand the function of an important class of enzymes. Contributed by Doug Auld.

## LUNGS REBUILT

Petersen TH, Calle EA, Zhao L, Lee EJ, Gui L, Raredon MB, Gavrillov K, Yi T, Zhuang ZW, Breuer C, Herzog E, Niklason LE. Tissue-engineered lungs for *in vivo* implantation. *Science* 2010;329:538–541.

**Abstract:** Because adult lung tissue has limited regeneration capacity, lung transplantation is the primary therapy for severely damaged lungs. To explore whether lung tissue can be regenerated *in vitro*, we treated lungs from adult rats using a procedure that removes cellular

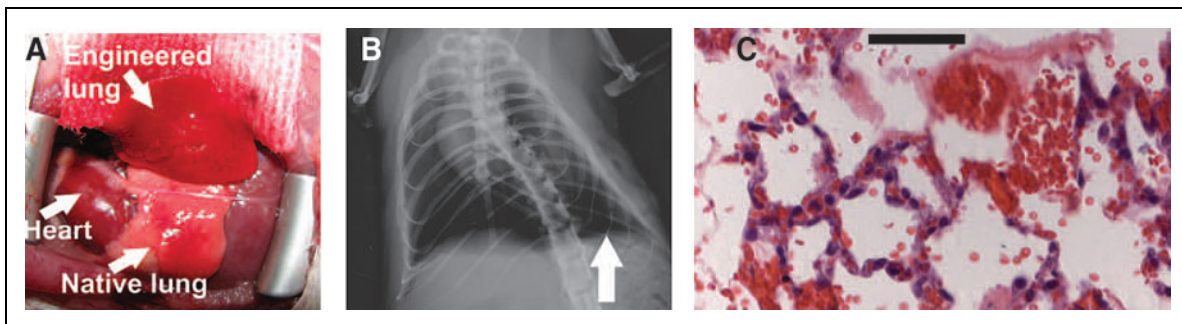
components but leaves behind a scaffold of extracellular matrix that retains the hierarchical branching structures of airways and vasculature. We then used a bioreactor to culture pulmonary epithelium and vascular endothelium on the acellular lung matrix. The seeded epithelium displayed remarkable hierarchical organization within the matrix, and the seeded endothelial cells efficiently repopulated the vascular compartment. *In vitro*, the mechanical characteristics of the engineered lungs were similar to those of native lung tissue, and when implanted into rats *in vivo* for short time intervals (45 to 120 minutes) the engineered lungs participated in gas exchange. Although representing only an initial step toward the ultimate goal of generating fully functional lungs *in vitro*, these results suggest that repopulation of lung matrix is a viable strategy for lung regeneration.



Schema for lung tissue engineering. **(A)** Native adult rat lung is cannulated in the pulmonary artery and trachea for infusion of decellularization solutions. **(B)** Acellular lung matrix is devoid of cells after 2 to 3 hours of treatment. **(C)** Acellular matrix is mounted inside a biomimetic bioreactor that allows seeding of vascular endothelium into the pulmonary artery and pulmonary epithelium into the trachea. **(D)** After 4 to 8 days of culture, the engineered lung is removed from the bioreactor and is suitable for implantation into **(E)** the syngeneic rat recipient.

**Commentary:** *A relatively wide range of artificial organs and prosthetic parts have become available, spanning from bone replacements made of inert materials, to skin grafts, to implanted artificial hearts. An organ that has remained difficult to repair is the lung, for which transplantation has been the only option and one associated with a very low success rate. The lung's exceedingly complex three-dimensional structure in combination with the complexities in tissue types represented, mechanical forces at play, and the fine balance required for successful gas exchange at the alveoli conspire to make the design of an artificial lung a nearly impossible task. In the present work published in Science, very significant progress*

*is reported toward the creation of a recipient-compatible artificial lung. In short, the new lung to be transplanted into the patient is being created by taking a lung from a donor cadaver, removing the lung cells while leaving the extracellular matrix/scaffold intact, seeding the scaffold with patient-derived epithelial and endothelial cells in a special bioreactor, and subsequently implanting the lung into the patient (see first figure). Rat lungs were used in these initial studies, which were designed to establish the protocol for stripping off the donor's cells, seeding the resulting matrix with the appropriate recipient cells, verifying the adequacy of the*



Implantation of engineered lungs into rats. **(A)** Tissue-engineered left lung was implanted into adult Fischer 344 rat recipient and photographed ~30 minutes later. **(B)** X-ray image of rat showing the implanted engineered left lung (white arrow) and the right native lung. **(C)** Hematoxylin and eosin stain of explanted lung. Red blood cells perfusing septa are evident, and some red blood cells are present in airspaces. Scale bar, 50  $\mu\text{m}$ .

## LITERATURE SEARCH AND REVIEW

reengineered lung with respect to tissue morphology and basic lung physical/mechanical properties, and finally, attempting to implant the lung into a rat recipient.

The authors were able to remove the cells by treatment with the zwitterionic detergent CHAPS and to show by a combination of staining and scanning techniques that the decellularized matrix retained its architecture while being devoid of donor cells (Figure 2 in the article). For seeding the matrix with cells, a special bioreactor was used to create a chest cavity and diaphragm type of environment: culture medium was fed into the pulmonary artery at physiological pressures, while a syringe pump was used to withdraw air from the surrounding space, thereby creating negative pressure that was accompanied by an increased liquid medium supply into the trachea. In this manner, cell seeding, supply of fresh medium, and removal of waste and debris could be achieved while providing mechanical stimuli close to those encountered in a live body environment. It was noted by the authors that during seeding and cell growth, the vascular perfusion created by the negative bioreactor pressure facilitated endothelial cell adhesion and allowed facile

clearance of epithelial secretions from the terminal regions of the airway tree. A spectrum of immunohistochemical staining tests, Western blot analyses, and mechanical characterization were performed to validate the reengineered organ (Figure 3 in the article). Finally, the new lung was implanted into a normal rat recipient whose own lung had been excised (see **second figure**). The replacement lung was easily attached to the recipient's bronchus and pulmonary vein and artery and was filled with blood within seconds upon flow establishment. The new lung was maintained inside the recipient animal for up to 2 hours, and at the end of the period, blood analyses were performed that showed that the implanted lungs were capable of gas exchange, albeit at somewhat reduced capacity. While this study represents a major proof of principle, a clinically tested human reengineered lung remains in the distant future. Key next steps toward achieving this ultimate goal include improvements in the recellularization procedure to ensure near-perfect integrity of the alveolar compartments and scaling up the procedure to animals larger in size and physiologically closer to humans. Contributed by Anton Simeonov.

---

## MORE LUNG

Ott HC, Clippinger B, Conrad C, Schuetz C, Pomerantseva I, Ikonomou L, Kotton D, Vacanti JP. Regeneration and orthotopic transplantation of a bioartificial lung. *Nat Med* 2010;16:927–933.

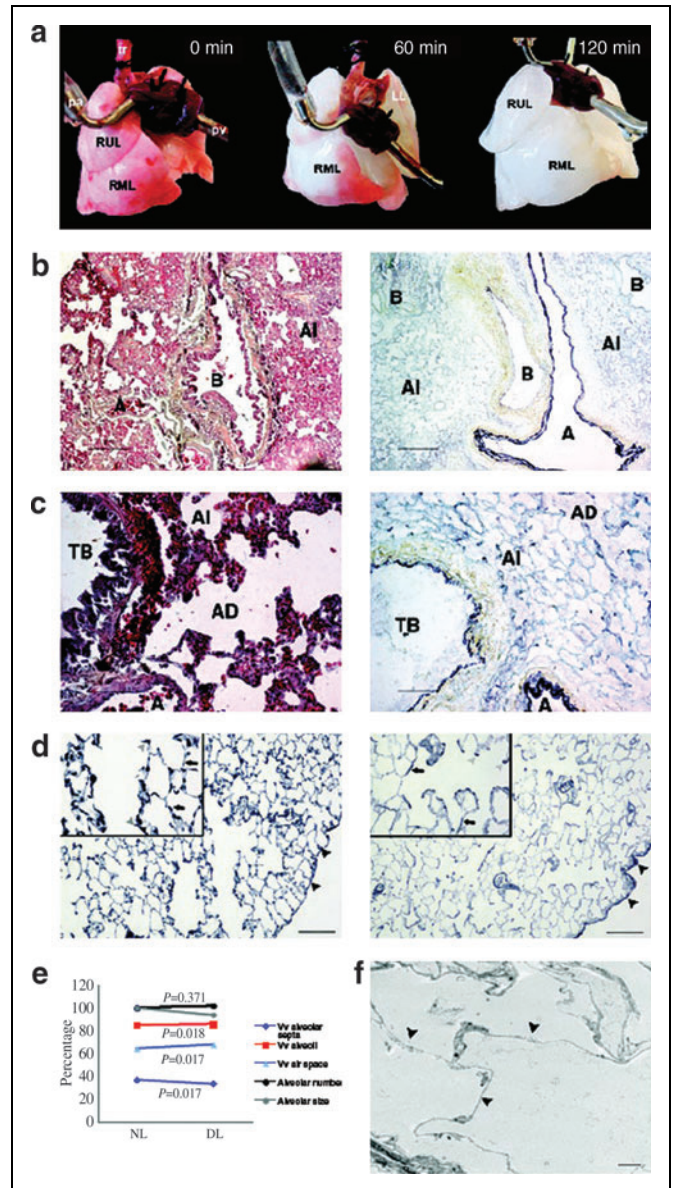
**Abstract:** About 2,000 patients now await a donor lung in the United States. Worldwide, 50 million individuals are living with endstage lung disease. Creation of a bioartificial lung requires engineering of viable lung architecture enabling ventilation, detergent perfusion and yielded scaffolds with acellular vasculature, airways and alveoli. To regenerate gas exchange tissue, we seeded scaffolds with epithelial and endothelial cells. To establish function, we perfused and ventilated cell-seeded constructs in a bioreactor simulating the physiologic environment of developing lung. By day 5, constructs could be perfused with blood and ventilated using physiologic pressures, and they generated gas exchange comparable to that of isolated native lungs. To show *in vivo* function, we transplanted regenerated lungs into orthotopic position. After transplantation, constructs were perfused by the recipient's circu-

lation and ventilated by means of the recipient's airway and respiratory muscles, and they provided gas exchange *in vivo* for up to 6 h after extubation.

**Commentary:** The work by Ott et al. provides an additional boost to the efforts to create replacement lung organs devoid of the deficiencies, dangers, and failure rates associated with direct lung transplants. Similar to the previous highlighted study (Petersen et al.), the authors utilized lungs from cadavers to remove the donor's cells, effectively creating a nonimmunogenic template that captured the organ's complexity and used it as a seeding substrate for the recipient's cells. Also in analogy with the report by Petersen et al., the major steps taken to create the new lung included establishment of procedures to remove the donor's cells, to reseed the scaffold with recipient's cells, to evaluate the regenerated lung, and to test-implant the organ into recipient animals (see **figure**). Interestingly, the cell removal procedure involved the use of sodium dodecyl sulfate (SDS), a detergent commonly used in denaturing protein gel electrophoresis.

The fact that the two teams optimized the decellularization procedure with two different detergents indicates that there may be other agents that could be used for cell removal, should there be a need to modify this step based on possible negative effects on the remaining matrix.

Three extensions of the investigation also mark this study as different from the work by Petersen et al. First, successful seeding and growth of human lung epithelial cells was demonstrated using the rat lung scaffold (although with increased culture time formation of solid tissue and path blockage was noted, likely due to lack of appropriate growth factors or incompatibility of the human cells with the rat matrix). Second, the studies with implanted reengineered lungs were continued for the extended period of 6 hours: development of pulmonary secretions over this longer post-graft period was noted, which indicates lack of complete compatibility and synchronization between the host pulmonary functions (mechanical forces from chest and diaphragm movement, blood and gas flow) and the implanted organ. Lastly, the authors performed scale-up investigations creating reengineered lungs for a range of species including primates, thus setting the stage for testing of human lungs. Contributed by Anton Simeonov.



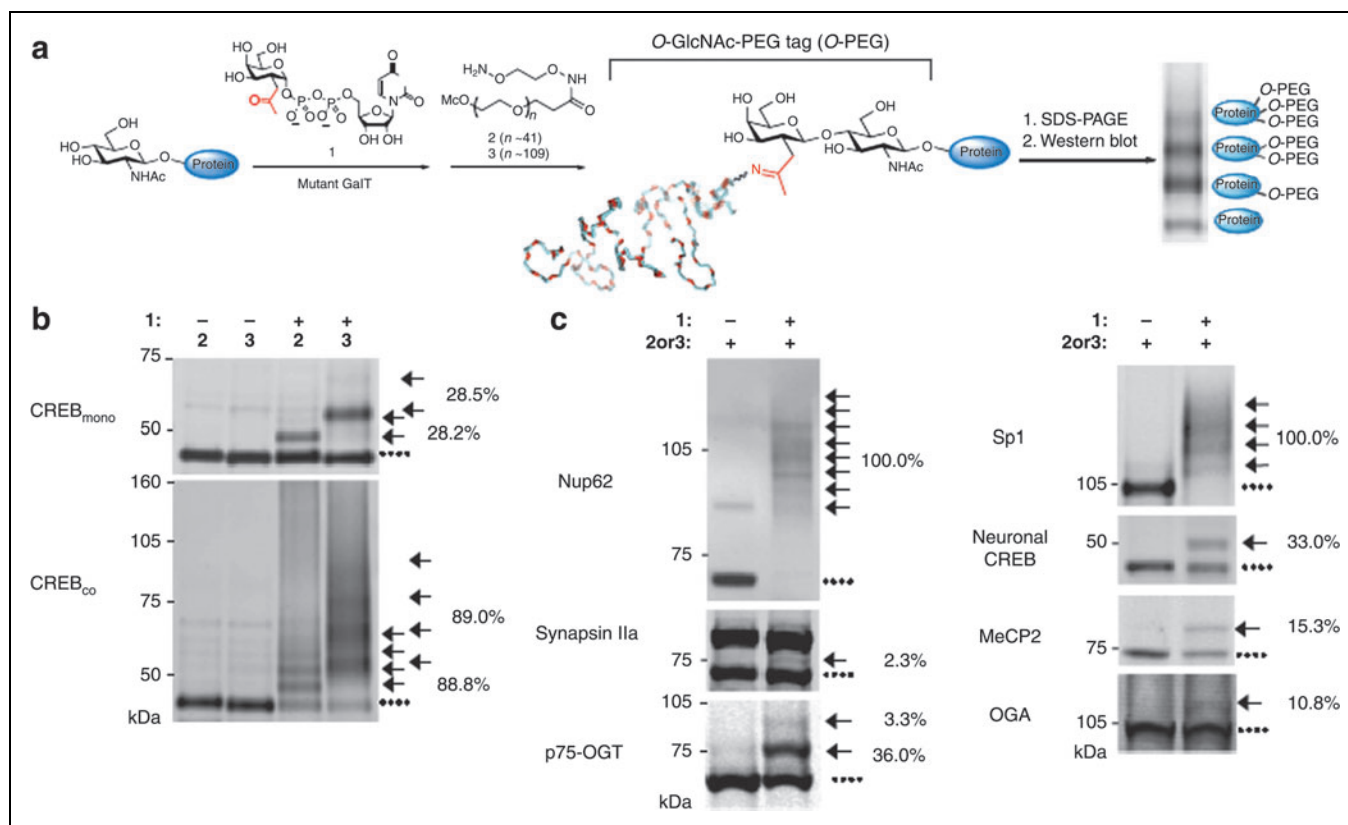
Perfusion decellularization of whole rat lungs. **(a)** Photographs of a cadaveric rat lung, mounted on a decellularization apparatus allowing antegrade pulmonary arterial perfusion. pa, pulmonary artery; pv, pulmonary vein; tr, trachea; RUL, right upper lobe; RML, right middle lobe; LL, left lobe. Freshly isolated lung (left), after 60 minutes of SDS perfusion (middle), and after 120 min of SDS perfusion (right). The lung becomes more translucent as cellular material is washed out first from apical segments, then from the middle segments and finally from the basal segments. **(b,c)** Corresponding Movat pentachrome staining of thin sections from parenchyma of native (left panels) and decellularized (right panels) rat lung showing preserved collagen (yellow), proteoglycans (blue) and elastic fibers (black). Low-power (top panels; scale bars, 200  $\mu$ m) and high-power fields (bottom panels; scale bars, 50  $\mu$ m) show preserved large (B, bronchus) and small conducting airway architecture (TB, terminal bronchus; AD, alveolar duct; AI, alveoli) and preserved large (>200  $\mu$ m) and small (50  $\mu$ m) arteries (A), in the absence of intact nuclei or cells in decellularized lungs. **(d)** Corresponding Verhoeff's elastic-tissue staining of thin sections from parenchyma of native (left) and decellularized (right) rat lung. Low and high-power fields (insets) show preservation of peripheral (black arrowheads), axial (gray arrowheads) and septal (black arrows) elastic fibers in decellularized lungs. Scale bars, 200  $\mu$ m. **(e)** Line chart summarizing morphometric and stereologic data from native (NL) and decellularized lungs (DL). Fractional volume (Vv) of alveolar septa decreased, whereas Vv of air space and alveoli increased with decellularization. Alveolar number expressed as percentage of that in native lung remained constant, whereas alveolar size slightly decreased (not significant). Error bars, s.d. **(f)** Transmission electron micrograph of decellularized rat lung (6000 $\times$ ) showing preserved basal membranes of alveolar septa (black arrowheads) in the absence of cells or nuclei. Scale bar, 2  $\mu$ m.

## CLIMB THE PEGS UP THE LADDER

Rexach JE, Rogers CJ, Yu S-H, Tao J, Sun YE, Hsieh-Wilson LC. Quantification of O-glycosylation stoichiometry and dynamics using resolvable mass tags. *J Med Chem* 2010;53:1238–1249.

**Abstract:** Mechanistic studies of O-GlcNAc glycosylation have been limited by an inability to monitor the glycosylation stoichiometries of proteins obtained from cells. Here we describe a powerful method to visualize the O-GlcNAc-modified protein subpopulation using

resolvable polyethylene glycol mass tags. This approach enables rapid quantification of *in vivo* glycosylation levels on endogenous proteins without the need for protein purification, advanced instrumentation or expensive radiolabels. In addition, it establishes the glycosylation state (for example, mono-, di-, tri-) of proteins, providing information regarding overall O-GlcNAc site occupancy that cannot be obtained using mass spectrometry. Finally, we apply this strategy to rapidly assess the complex interplay between glycosyla-



Mass-tagging strategy for quantifying O-GlcNAc glycosylation levels on specific proteins. **(a)** Schematic of the approach. O-GlcNAc-modified proteins are chemoenzymatically labeled using the UDP-ketogalactose analog 1 and an engineered GalT enzyme and then reacted with an aminoxy-functionalized PEG mass tag (2 or 3). This approach enables facile visualization of O-GlcNAc-glycosylated species upon SDS-PAGE and immunoblotting with antibodies against proteins of interest. **(b)** Validation of the approach using CREB<sub>mono</sub> and CREB<sub>co</sub>. CREB<sub>mono</sub> was 28.2% glycosylated and existed primarily in the monoglycosylated state, whereas CREB<sub>co</sub> was 88.8% glycosylated and present in multiply glycosylated forms. **(c)** *In vivo* O-GlcNAc stoichiometries vary significantly even among proteins with similar functions. Cell lysates (100 μg) from 293T cells (source of Sp1), adult rat brain (source of MeCP2, Nup62 and synapsin Ia (upper band) and IIa (lower band), embryonic neuronal cultures (source of CREB and OGA) or purified p75-OGT (0.43 μg) from Sf9 cells were subjected to chemoenzymatic labeling, SDS-PAGE, and immunoblotting with antibodies against the indicated proteins.

tion and phosphorylation and discover an unexpected reverse ‘yin-yang’ relationship on the transcriptional repressor MeCP2 that was undetectable by traditional methods. We anticipate that this mass-tagging strategy will advance our understanding of O-GlcNAc glycosylation, as well as other post-translational modifications and poorly understood glycosylation motifs.

**Commentary:** *The targets and functional contributions of O-glycosylation events (particularly in terms of the interrelationship with protein phosphorylation) have been difficult to study. The methods that have existed to date are arduous and not applicable to in vivo settings. Here, the Hsieh-Wilson lab offers a simple but elegant method to study not only targets of O-glycosylation but the stoichiometry of the event as well (see figure). The method revolves around the ability to chemically modify a ketone-based version of GlcNAc after it has already post-translationally modified its protein target via chemical ligation to an aminoxy-functionalized PEG mass tag of two separate sizes (n of approximately 41 or 109). The result is a protein with a post-translational appendage that is large enough to mass-shift the protein on SDS-PAGE to an easily quantifiable level. The authors put three caveats on the method: (1) the enzymatic labeling must go to completion; (2) the PEG tag can not interfere with the*

*Western blotting; and (3) the labeling must be linear across multiple stoichiometries. After validating that these three criteria were met, the authors used the working technology to resolve several unanswered questions surrounding O-GlcNAc biology. Among their findings was the fact that O-GlcNAc stoichiometries vary greatly in vivo and can co-exist with protein phosphorylation. Further, a comparative analysis of O-GlcNAc levels in various tissues found that glycosylation levels were higher in rat brain tissues relative to rat liver tissue. Finally, the authors sought to determine the functional interplay between phosphorylation events and glycosylation events in vivo. Using this technology, they determined that the functionally relevant phosphorylation of CREB pS133 was not affected by the presence or absence of O-GlcNAc. A similar investigation was undertaken for the transcriptional repressor MeCP2. Here, GlcN induction was found to decrease the percentage of phosphorylation events at a specific site (Ser80) in non-O-GlcNAc-modified MeCP2 while increasing it in O-GlcNAc-modified MeCP2. Overall, the results from the in vivo analyses using this novel technique highly suggest a complicated relationship between these two important post-translational modifications. Undoubtedly, the use of these resolvable mass tags will greatly enable the research community to further unravel these complicated questions. Contributed by Craig Thomas.*

## SYNERGY: WHAT CAN YOU FIND?

Farha MA, Brown ED. Chemical probes of *Escherichia coli* uncovered through chemical-chemical interaction profiling with compounds of known biological activity. *J Chem Biol* 2010;17: 852–862.

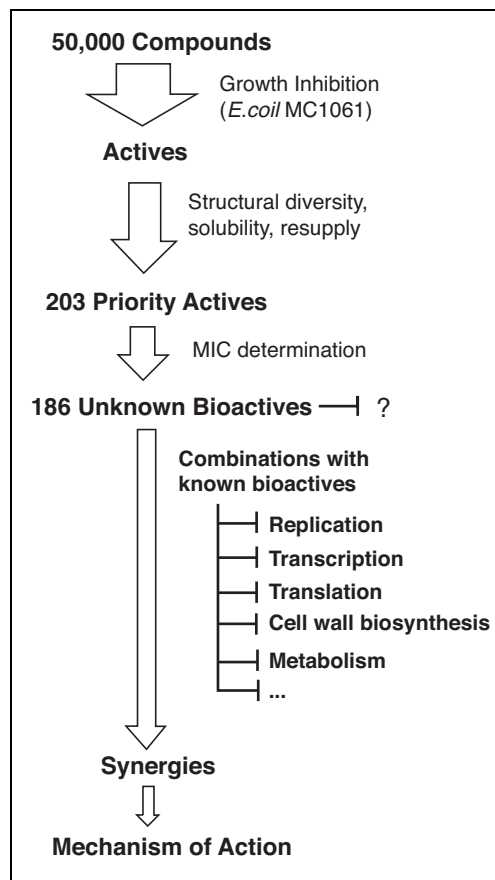
**Abstract:** While cell-based screens have considerable power in identifying new chemical probes of biological systems and leads for new drugs, a major challenge to the utility of such compounds is in connecting phenotype with a cellular target. Here, we present a systematic study to elucidate the mechanism of action of uncharacterized inhibitors of the growth of *Escherichia coli* through careful analyses of interactions with compounds of known biological activity. We studied growth inhibition with a collection of 200 antibacterial compounds when systematically combined with a panel of 14 known antibiotics of diverse mechanism and chemical class. Our work revealed a high frequency of synergistic chemical interactions where the interaction profiles were unique to the various compound pairs. Thus, the work revealed that chemical-chemical interaction data provides a fingerprint of biological

activity and testable hypotheses regarding the mechanism of action of the novel bioactive molecules. In the study reported here, we determined the mode of action of an inhibitor of folate biosynthesis and a DNA gyrase inhibitor. Moreover, we identified eight membrane active compounds, found to be promiscuously synergistic with known bioactives.

**Commentary:** *Assays strategies based on a forward chemical genomic approaches have to address the difficult step of determining the mechanism of action of compounds identified in these efforts. Ferreting out the molecular target of a small molecule found within a phenotypical screen typically involves laborious efforts surrounding various ligation or affinity techniques or protein expression-based cellular arrays that provide clues to the protein of interest in competitive growth assays. Several of the commentaries that appear in ADDT revolve around strategies to decipher the molecular target(s) of agents found within cell-based assays. This contribution by Farha and Brown suggests an interesting approach to shed light on novel agent’s mechanism of action through the use of a matrix screening approach*

## LITERATURE SEARCH AND REVIEW

to look for synergies between compounds of unknown activity and those with well-characterized biological activity. A prioritized list containing 186 actives of unknown function was derived from a screen against 50,000 compounds using an assay for growth inhibition of the *E. coli* strain MC1061 (see figure). Fourteen known bioactives that inhibit bacterial growth by targeting key processes such as replication, transcription, translation, or cell wall biosynthesis were tested to determine if any of them modulated the activity of the unknown compounds in a synergistic manner. To reduce the complexity of the combination testing, a two-dose matrix was constructed to test all 2,604 pairwise interactions using two sublethal concentrations of the known bioactives. A growth ratio index, which was calculated from the average percent growth of the combinations divided by the growth in the presence of bioactives alone, was used to determine synergy. The sublethal dose controls showed ~85% growth relative to untreated controls and a growth ratio of 0.25 (e.g., 75% growth inhibition) was considered significant. The technical details for the combination profiling screen were appropriately defined and the “actives” from this screen were based upon true synergy rather than additive effects and it was determined that 45 of the 186 compounds had synergistic interactions with the known bioactive agents. Current understanding of signal-transduction pathways or cell-cycle mediators may provide clues as to the new agents’ mode of activity and the authors home in on two agents. First was a previously described dihydrofolate reductase inhibitor that was found to synergize with the tetrahydrofolate biosynthesis inhibitor sulfamethoxazole. The second was a quinolone-based small molecule that the authors assumed was a DNA gyrase inhibitor based upon structural precedence. The authors were able to demonstrate that this agent did inhibit the *E. coli* gyrase at high concentrations and synergized with norfloxacin, which is a known, highly potent gyrase inhibitor. It is suggested that the novel agent synergizes with norfloxacin due to binding gyrase at an orthogonol site and/or due to a secondary activity at some other cellular target. Often in such profiling studies one identifies a number of “pan-active” compounds and in these studies eight compounds appeared to be promiscuously synergistic. These agents were found to depolarize the cytoplasmic membrane and cause a hyper-permeabilization event. Ultimately, the use of combination synergies data alone to identify the



Summary of the approach to understand mechanism(s) of action of a novel active chemical matter. Synergies uncovered through combination studies, in which priority actives are systematically combined with a panel of known bioactive compounds of diverse mechanism and chemical class, provide clues about the pathways and targets.

cellular target of agents found in phenotypic screens wasn't realized in this contribution. However, the theory is sound and it's likely only a matter of time before this technique yields impressive results. Contributed by Craig Thomas and Doug Auld.

## EPIGENETIC ASSAY BY EPITOPE MASKING

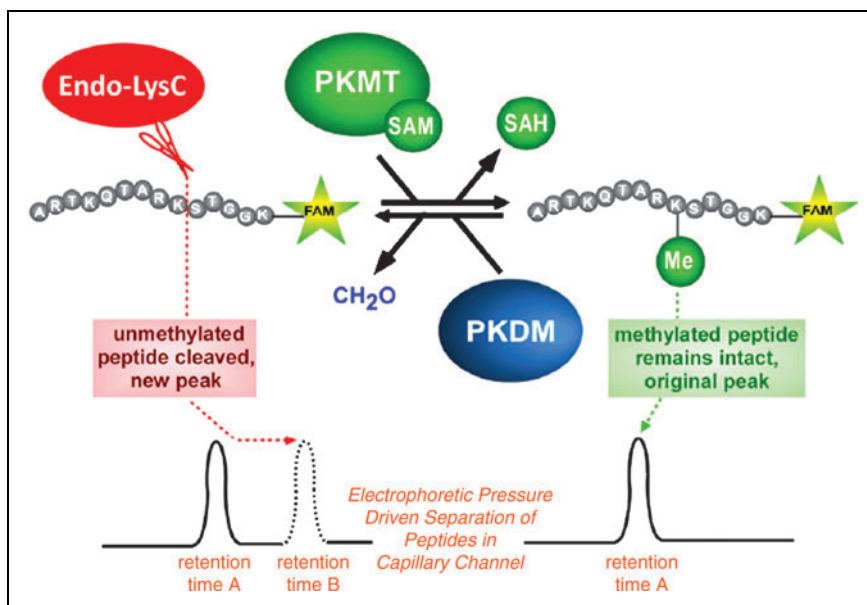
Wigle TJ, Provencher LM, Norris JL, Jin J, Brown PJ, Frye SV, Janzen WP. Accessing protein methyltransferase and demethylase enzymology using microfluidic capillary electrophoresis. *Chem Biol* 2010;17:695–704.

**Abstract:** The discovery of small molecules targeting the >80 enzymes that add (methyltransferases) or remove (demethylases) methyl marks from lysine and arginine residues, most notably present in histone tails, may yield unprecedented hemotherapeutic agents and

facilitate regenerative medicine. To better enable chemical exploration of these proteins, we have developed a highly quantitative microfluidic capillary electrophoresis assay to enable full mechanistic studies of these enzymes and the kinetics of their inhibition. This technology separates small biomolecules, i.e., peptides, based on their charge-to-mass ratio. Methylation, however, does not alter the charge of peptide substrates. To overcome this limitation, we have employed a methylation-sensitive endoproteinase strategy to separate methylated from unmethylated peptides. The assay was validated on a lysine methyltransferase (G9a) and a lysine demethylase (LSD1) and was employed to investigate the inhibition of G9a by small molecules.

**Commentary:** The epigenetic code is represented by DNA methylation and a variety of post-translational modifications of histone proteins. Among those protein modifications, histone methylation and demethylation, mediated by methyltransferases and demethylases, respectively, are of great interest due to their role in transcriptional regulation and mounting implications in a range of diseases (Spannhoff et al., *ChemMedChem*, 2009;4:1568–1582). One of the common methylation sites is on lysine residues, and lysine methyltransferases utilize cofactor *S*-adenosylmethionine (SAM) to achieve methyl group transfer. Current assays for protein lysine methylation are limited in their utility by factors such as radioactivity-associated hazards or reagent interference (Bissinger et al., *Chem Biol*, 2010;17:677–678).

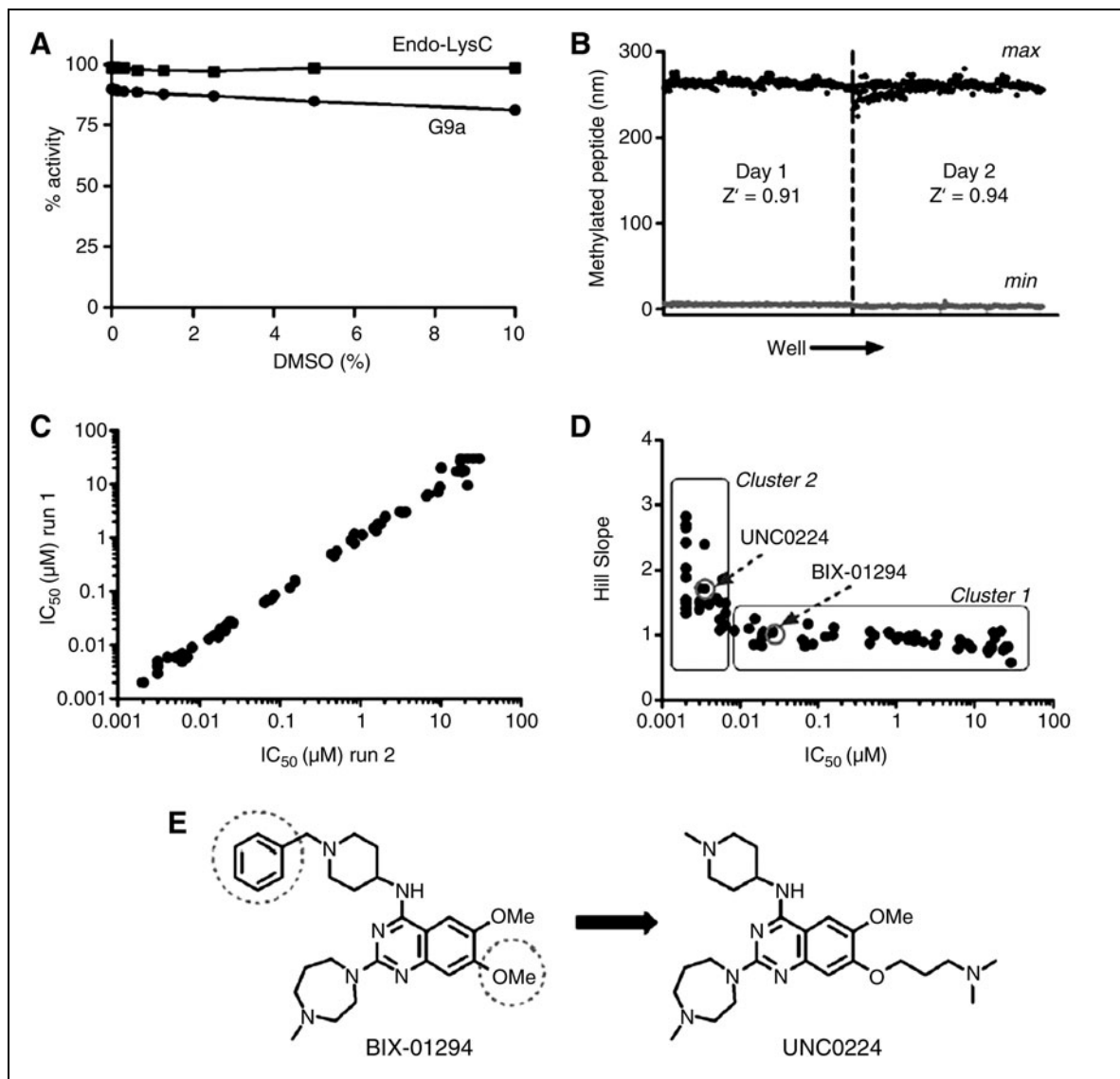
Recently, Wigle et al. validated a high-throughput friendly microfluidic capillary electrophoresis (MCE) assay using a lysine methyltransferase, G9a, and a lysine demethylase, LSD1. Methylation does not lead to a charge change in amino acid residues of histone peptides. Thus, in an approach similar to epitope masking assays, the authors utilized a methylation sensitive protease, endoproteinase-LysC (Endo-LysC), to differentiate methylated from unmethylated peptides based on separation of the peptides from proteolysis (see **first figure**). Endo-LysC was expected to only cleave peptides with unmethylated lysines, and methylated and unmethylated peptides were successfully separated on the electrophoretic system used (Caliper EZ Reader II). Adding Endo-LysC to mixtures of fluorescein-labeled methylated and unmethylated peptides and allowing the cleavage to proceed to completion resulted in two peaks, corresponding to the methylated full-length peptide (at retention A in the **first figure**) and cleavage product



**Methylation-sensitive endoproteinase-linked microfluidic capillary electrophoresis assay concept.** Protein lysine methyltransferases (PKMT) methylate substrate peptides, which prevents proteolysis of the peptide at the target lysine by endoproteinase-LysC. Protein lysine demethylases (PKDM) demethylate peptide substrates and render it susceptible to proteolysis by endoproteinase-LysC. The cleaved versus uncleaved peptides are separable on a Caliper Life Sciences EZ Reader II, which “sips” nanoliter-sized samples from reactions in microplate wells into a capillary channel on a quartz chip. A pressure driven flow and electric current are used to resolve the peptides based on their charge-to-mass ratio. The incorporation of a fluorescein-based tracer enables the detection of the peptides at the end of the capillary channel. This assay format is compatible with 384-well microplates, can be performed in volumes as low as 10–15  $\mu$ l, and is a widely used technology in drug discovery.

of the unmethylated peptide (at retention B in the **first figure**), each carrying a different net charge. The authors further designed histone peptide substrates for both G9a and LSD1, and optimized their performance by varying fluorophore attachment point on the peptides, peptide length, and premethylation of selective lysine residues. Subsequently, an Endo-LysC-coupled MCE assay was configured for G9a small molecule screening in a 384-well format. After examining the assay robustness (see **second figure**, panels A and B), a further 83 quinazoline-based inhibitors were assessed for potency (see **second figure**, panels C and D). In addition, the system was used to investigate enzyme kinetics and probe small molecule inhibition mode. Performing the assay in a time-dependent titration mode, the  $K_m$  of G9a peptide substrate and cofactor SAM were obtained, and UNC0224 (see **second figure**, panel E) was found to be a peptide substrate competitive inhibitor with a  $K_i$  of 1.6 nM.

Despite the method's dependence on a specialized instrument, this assay is highly relevant because it permits execution of kinetic studies



**Configuring the G9a MCE assay for small molecule screening.** (A) DMSO sensitivity curves for G9a and Endo-LysC. (B) Statistical evaluation of the maximum and minimum signal control reactions of the assay over the course of 2 days results in an average Z' factor of 0.92 and CVs of less than 2%. (C) Graphical representation of the  $IC_{50}$  values measured for 83 small molecules over the course of two independent runs of the assay indicates excellent correlation between dose response assays. (D) A plot of Hill Slope versus the  $IC_{50}$  measured indicates two major clusters of compounds: (1) Compounds with Hill Slope of roughly 1 and potency >5 nM are rank-ordered by the assay, (2) while compounds with Hill Slope >1 and  $IC_{50}$  <5 nM have reached the potency detection limit of the assay. UNC0224 and BIX-01294 are indicated on the plot. The observation that  $IC_{50}$  values of as little as 2 nM can be measured is likely a reflection of the fraction of active G9a among the 10 nM enzyme added. (E) Structure guided design of UNC0224 from the BIX-01294 quinazoline template.

that other methyltransferase assays do not allow, and it has the potential to be used for a wide range of methyltransferases and demethylases. Variation of the assay's last step by utilizing other

detection methods, such as fluorescence polarization or FRET, can be explored so that the principle can be applied without the need of specialized instruments. Contributed by Wendy Lea.

## THREADING THROUGH NANO

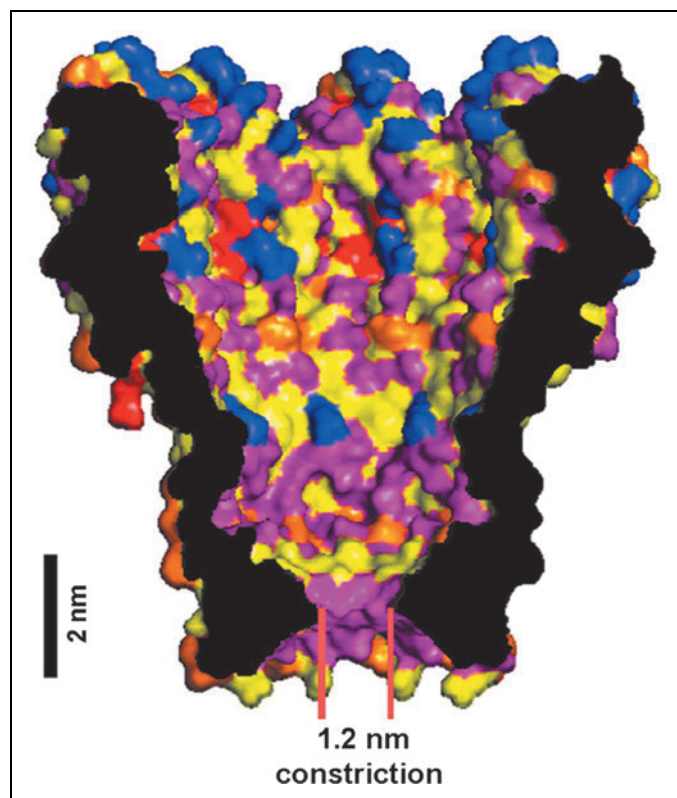
Derrington IM, Butler TZ, Collins MD, Manrao E, Pavlenok M, Niederweis M, Gundlach JH. Nanopore DNA sequencing with MspA. *PNAS* 2010;107:16060–16065.

**Abstract:** Nanopore sequencing has the potential to become a direct, fast, and inexpensive DNA sequencing technology. The simplest form of nanopore DNA sequencing utilizes the hypothesis that individual nucleotides of single-stranded DNA passing through a nanopore will uniquely modulate an ionic current flowing through the pore, allowing the record of the current to yield the DNA sequence. We demonstrate that the ionic current through the engineered *Mycobacterium smegmatis* porin A, MspA, has the ability to distinguish all four DNA nucleotides and resolve single-nucleotides in single-stranded DNA when double-stranded DNA temporarily holds the nucleotides in the pore constriction. Passing DNA with a series of double-stranded sections through MspA provides proof of principle of a simple DNA sequencing method using a nanopore. These findings highlight the importance of MspA in the future of nanopore sequencing.

**Commentary:** *In the quest for cheaper and faster next-generation sequencing technologies, nanopore sequencing is a relatively early-stage method that nevertheless carries significant promise. As a technique, it has the potential to provide a direct readout of the individual bases comprising the DNA template as they pass through nanopores via electrophoretically driven transport: the residual ion current associated with each passing nucleotide can be recorded and used to derive sequence information. Multiple issues surrounding nanopore sequencing need to be resolved before it can become a reality. These include the reliable manufacturing of the nanopore device, selection of the nanopore material itself, and perfecting the signal collection modality. In the work by Derrington and colleagues, the bacterial protein porin A (MspA) from *Mycobacterium smegmatis* is used as the nanopore constituent material (see first figure). Previous nanopore sequencing studies have used the protein  $\alpha$ -hemolysin; however, among the deficiencies noted have been the relatively large length of its pore (5 nm), which limits the signal generated from the ion current, and the associated need to mutate too many amino acid residues on the protein in order to change the nanopore properties. In contrast, MspA provides a relatively shallow pore of approximately 0.5 nm, and previous mutagenesis work has led to the removal of*

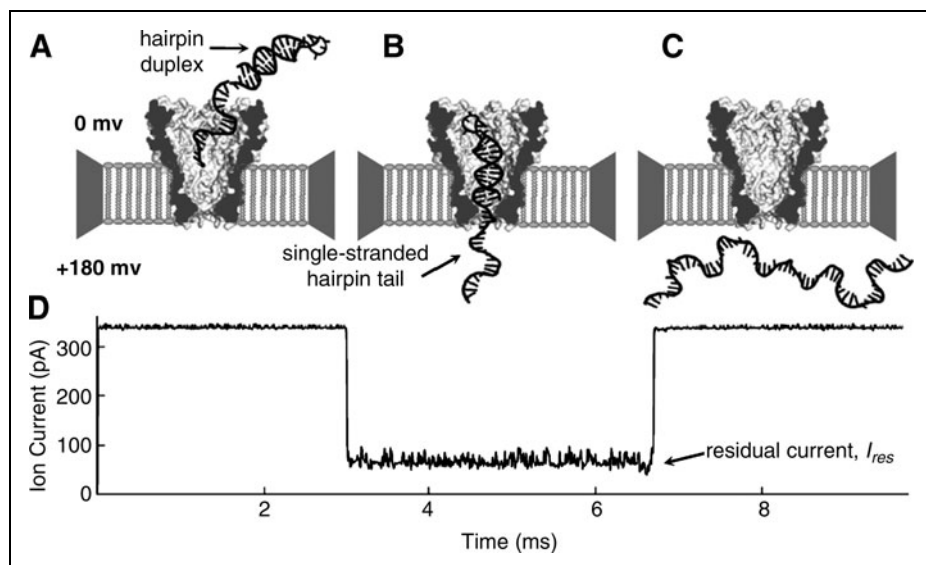
*interfering negatively charged aspartate residues from the protein surface surrounding the pore.*

*A major challenge in nanopore sequencing relates to the rate of the test strand passing through the pore and the associated rate of signal acquisition: if the DNA translocates too fast, the ion current changes associated with each passing nucleotide tend to become smaller and*



Crystal structure of MspA. The cross-sectional view through M1-NNNMspA's structure using a space-filling model displays the classes of amino acids: red are positively charged; blue are negatively charged; purple are polar; yellow are hydrophobic-aliphatic; orange are hydrophobic-aromatic. The single constriction, with dimensions similar to that of a single-nucleotide, makes MspA a good candidate for nanopore DNA sequencing techniques.

## LITERATURE SEARCH AND REVIEW



DNA translocation through the nanopore MspA. The cartoon depicts DNA translocation through MspA and the resulting residual current. **(A)** The positive voltage attracts the negatively charged hairpin DNA into the pore. **(B)** The DNA threads through the pore until the wider hairpin duplex prevents further translocation. **(C)** After a few milliseconds the hairpin dissociates allowing for complete translocation. **(D)** The resulting current trace associated with the above cartoon shows that the hairpin DNA present in the pore allows a residual current,  $I_{res}$ , until the hairpin duplex dissociates.

more difficult to resolve. In the present study, the authors were able to retard DNA translocation by generating a special hairpin-containing structure that contained the test sequence in the middle (see second figure). After careful optimization of the flanking sequences and structures, the MspA nanopores, which consisted of a hairpin unit on the 5' end and a poly(A) tail on the 3' end, were shown to provide unambiguous recognition of the four nucleobases (Figures 3 and 4 in the article). Subsequently, a sample containing an unknown five-nucleotide stretch was sequenced successfully (Figure 5 in the

article). While the study validates MspA as a new promising material for nanopore sequencing, a new bottleneck in this process now needs to be resolved: in order to slow down the test DNA, the method requires that a special nucleic acid structure be generated via a combination of enzyme treatment steps, such as restriction digestion and ligation. The implementation of such a protocol on a massive scale with real-life sequencing samples will undoubtedly require extensive optimization and will likely lower the attractiveness of this new sequencing method. Contributed by Anton Simeonov.

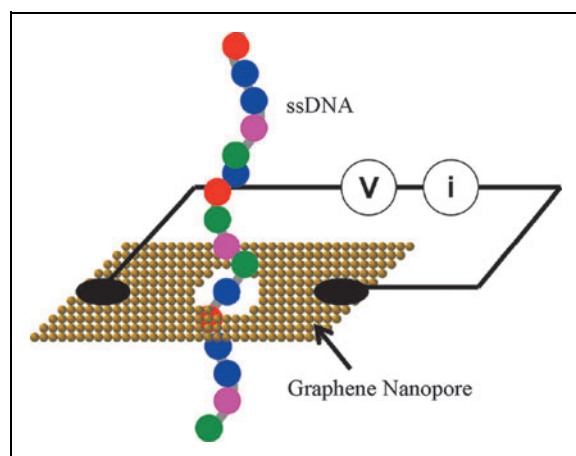
## NANOSEQUENCING CALCULATED

Nelson T, Zhang B, Prezhdov OV. Detection of nucleic acids with graphene nanopores: *ab initio* characterization of a novel sequencing device. *Nano Lett* 2010;10:3237–3242.

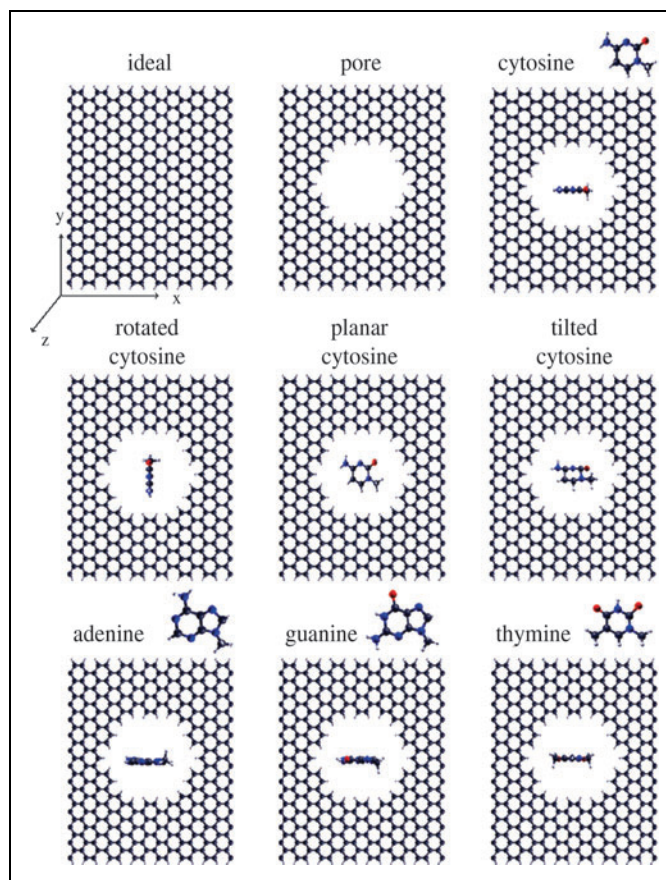
**Abstract:** We report an *ab initio* density functional theory study of the interaction of four nucleobases, cytosine, thymine, adenine, and guanine, with a novel graphene nanopore device for detecting the base sequence of a single-stranded nucleic acid (ssDNA or RNA). The nucleobases were inserted into a pore in a graphene nanoribbon, and the electrical current and conductance spectra were calculated as

functions of voltage applied across the nanoribbon. The conductance spectra and charge densities were analyzed in the presence of each nucleobase in the graphene nanopore. The results indicate that due to significant differences in the conductance spectra the proposed device has adequate sensitivity to discriminate between different nucleotides. Moreover, we show that the nucleotide conductance spectrum is affected little by its orientation inside the graphene nanopore. The proposed technique may be extremely useful for real applications in developing ultrafast, low-cost DNA sequencing methods.

**Commentary:** As outlined in the previous commentary (Derrington et al.), nanopore sequencing is a young technology facing several challenges, including the nanopore building material selection. Nelson et al. tackle the problem computationally by using ab initio density functional theory analysis to evaluate the potential of graphene nanopores to serve as discriminators of single-base differences in test DNA. While protein-based nanopores are found to be attractive due to their “bioinspired” nature of base recognition and the possibility for targeted pore surface modification via site-directed mutagenesis, inorganic type surfaces are also being evaluated by research teams due to their superior mechanical properties, longer shelf life, and the potential for inexpensive manufacture. In this report, a device consisting of graphene nanopores fabricated onto a silica substrate is proposed (see **first figure**). The authors calculated the electronic structure and states of nine model systems representing different base interactions with the pore geometry (see **second figure**). First, a cytosine was fitted through the pore and the associated conductance and current were calculated; then, the remaining three bases were analyzed, also allowing for different rotational configurations. It was determined that the graphene pore could discriminate the four bases. Next, the authors performed detailed calculations of the complete conductance and current spectra as individual nucleotides passed through the pore and concluded that the current signatures anticipated from the device were of sufficient magnitude to be detected. Furthermore, it was shown through these calculations that the indi-



Proposed nanopore sensor consists of a graphene nanopore embedded in SiO<sub>2</sub> (not pictured). Single-stranded DNA translocates through the nanopore. The current flow is perpendicular to the DNA backbone.



Model systems used for analysis. Gray, white, blue, and red spheres represent carbon, hydrogen, nitrogen, and oxygen, respectively. First row: Starting with an ideal GNR (left) we first created a 1.45-nm pore in the ribbon (center). Then cytosine was placed in the pore (right). Second row: Orientation of the nucleobase was investigated using cytosine. The cytosine molecule was rotated about the z-axis by 90° (left). Cytosine was then placed in a planar configuration by rotating 90° about the x-axis (center) followed by an intermediate tilted configuration achieved by a 45° rotation about the x-axis (right). Bottom row: The three remaining nucleobases adenine (left), guanine (center), and thymine (right) were then placed in the pore.

*vidual bases' signatures were independent of the sequence context and that the signal was not affected by the polarity of the DNA strand as it passed through the pore. The calculations presented in this study argue strongly in favor of a graphene-based sequencing device and provide the basis for evaluation of a future prototype. Contributed by Anton Simeonov.*